Physics of Fluids

Non-monotonic viscous dissipation of bouncing droplets undergoing off-center collision

Cite as: Phys. Fluids **31**, 052004 (2019); https://doi.org/10.1063/1.5088544
Submitted: 11 January 2019 . Accepted: 30 April 2019 . Published Online: 23 May 2019

Chengming He (何成明), Xi Xia (夏溪), and Peng Zhang (张鹏)

Physics of Fluids ARTICLE scitation.org/journal/phf

Non-monotonic viscous dissipation of bouncing droplets undergoing off-center collision

Cite as: Phys. Fluids 31, 052004 (2019); doi: 10.1063/1.5088544
Submitted: 11 January 2019 • Accepted: 30 April 2019 •
Published Online: 23 May 2019

Chengming He (何成明), Xi Xia (夏溪), and Peng Zhang (张鹏)[a)]

AFFILIATIONS

Department of Mechanical Engineering, The Hong Kong Polytechnic University, Hung Hom, Kowloon 999077, Hong Kong

[a)]Author to whom correspondence should be addressed: pengzhang.zhang@polyu.edu.hk

ABSTRACT

The off-center collision of binary bouncing droplets of equal size was studied numerically by a volume-of-fluid method with two marker functions, which has been justified and validated by comparing with available experimental results. A nonmonotonic kinetic energy (KE) recovery with varying impact parameters was discovered. This can be explained by the prolonged entanglement time and the enhanced internal-flow-induced viscous dissipation for bouncing droplets at intermediate impact parameters, compared with those at smaller or larger impact parameters. The distribution of the local viscous dissipation rate (VDR) in the droplet interior shows two major concentration areas, and the competition between these two concentration areas accounts for the nonmonotonic viscous dissipation with varying impact parameters. The nonmonotonic KE recovery with varying impact parameters can also be attributed to the competition between the VDR induced by normal strains and shear strains. The nonmonotonicity was further numerically verified for wider ranges of parameters, and a practically useful formula was proposed to correlate the KE dissipation factor with the impact parameter for various Weber numbers and Ohnesorge numbers.

I. INTRODUCTION

Binary droplet collision[1–8] had been studied substantially to probe more complicated physics in the context of various spray processes, such as cloud and raindrop formation,[9,10] dense spray combustion,[11,12] droplet manipulation in microfluidics,[13,14] and various applications involving functional interfaces[15–20] in materials science.

The investigation of droplet collision could date back to the study on cloud aerosols, which was aimed to explain the mechanism of raindrop formation. Historically, studying the raindrop formation raised some arguments about which mechanism plays the dominant role,[9,10] between the fragmentation of large droplets and the coalescence of minute droplets. It then spawned the early studies[3] on the collision between two water droplets in standard atmosphere environments, resulting in the discovery of two collision outcomes, coalescence and separation. However, raindrops might have opposite charges[21] so that they tend to bounce off upon collision and their distributions of size, number density, and velocity are accordingly influenced.

In recent years, to understand the sprays of liquid fuels in combustion conditions, research efforts have been devoted to the collision between two hydrocarbon droplets[4,7] in various gaseous environments, and most relevant studies were focused on droplet coalescence[1,3,22] and the subsequent internal mixing.[23–27] Although not being sufficiently studied, interesting phenomena were also observed for droplet bouncing; for example, bouncing was found to occur to only fuel droplets[4,7] but not water droplets in standard atmosphere environments. Furthermore, the collision outcomes can be significantly affected by the gas environment; specifically, increasing the gas pressure promotes droplet bouncing and decreasing the gas pressure promotes droplet coalescence.[7,28,29] Given the elevated pressure[7,29] in real combustion chambers, droplet bouncing is a prominent collision outcome and of great significance in dense spray combustion. It has been verified both experimentally and numerically[30–32] that a high pressure environment favors droplet bouncing in impinging jets.

Compared with the extensively studied droplet coalescence and separation,[1,2,4,5,7,22,26] binary droplet bouncing has been investigated by only a few studies. Al-Dirawi and Bayly[33] experimentally studied the binary collision between identical droplets with different viscosities and proposed an improved model for the prediction of bouncing regimes in the nomogram of Weber number and impact parameter space. Farokhirad *et al.*[34] and Attarzadeh and

Dolatabadi[35] numerically studied the phenomenon of coalescence-induced binary droplets jumping on homogeneous and heterogeneous superhydrophobic surfaces. The dynamics of interfacial gas layer[36] and viscous effects[37] on the bouncing-to-merging transition in droplets impacting on the liquid film were studied, in which the droplet impacting on the liquid pool was a special case of binary droplet collision with infinite size ratio. Blanchette[38] proposed a model to describe droplets bouncing on an oscillated reservoir with various bouncing modes. Pan *et al.*[6] studied the evolution of energy budget for head-on bouncing between binary droplets of equal size both experimentally and numerically. Tang *et al.*[8] experimentally observed the head-on bouncing between binary droplets of unequal sizes. The present study attempts to focus on the three-dimensional (3D) off-center droplet bouncing, which is more practical and general than the axisymmetric head-on case. Chen and Yang[39] developed a thickness-based adaptive mesh refinement approach based on the Volume-of-fluid (VOF) method to simulate 3D off-center droplet bouncing. Hu *et al.*[40] used a VOF method to numerically study 3D off-center bouncing of alumina droplets. In order to emphasize the influence of off-center collision (measured by the impact parameter) on droplet bouncing, the present study limits its scope to droplets of equal size to avoid possible complexity introduced by variable size ratio, although the size ratio effects have been demonstrated to be important to droplet collision in other studies.[8,25,26,41,42]

The present study employs the 3D volume-of-fluid (VOF) method[43,44] to simulate off-center collisions of two droplets. To improve computational efficiency and avoid numerical coalescence caused by possible coarse mesh, we adopted the VOF method with two marker functions[40,45] to track the liquid-gas interfaces. A major challenge of simulating droplet collision lies in the inability of the Navier-Stokes equations in capturing the rarified gas effects and the van der Waals force[46] within the gas film between two colliding droplets, thus prohibiting the accurate prediction of droplet coalescence. Although Li[47] reported preliminary success in numerically predicting droplet coalescence by implementing Zhang and Law's solution[46] for the rarefied gas film, it is still computationally expensive to resolve the interface mesh to the scale of $O(10)$ nm, especially in 3D simulations. Fortunately, the current simulation of droplet bouncing does not involve treatments of interface rupture and is less numerically demanding than predicting droplet coalescence.

In Lagrangian simulations of sprays,[48–52] few previous works have investigated in detail the variation of the kinetic energy (KE) loss in off-center droplet bouncing. The classical O'Rourke model[51,53] only considers droplet coalescence and grazing separation, in which droplet bouncing is treated as grazing collision with the kinetic energy dissipation factor $f_E \equiv 1 - \mathrm{KE_a}/\mathrm{KE_b} = 0$, where $\mathrm{KE_b}$ and $\mathrm{KE_a}$ represent the kinetic energy of droplets before and after the collision, respectively. In lieu of O'Rourke's assumption, Zhang *et al.*[30] used an approximation of $f_E = 0.5$ suggested by Jiang *et al.*'s experiments.[4] The numerical simulation of Chen *et al.*[54] found that the normalized kinetic energy loss at the maximum droplet deformation decreases monotonically with increasing B. Zhang and Zhang[55] numerically studied the kinetic energy recovery and viscous dissipation of bouncing droplets undergoing head-on collision.

The present study attempts to promote both the physical understanding on the viscous dissipation of bouncing droplets undergoing off-center collision and the applications of the droplet bouncing modeling in Lagrangian simulations of sprays. The numerical methodology and validations are given in Sec. II, followed by the preliminary analysis of the bouncing phenomenon and energy budget in Sec. III. The detailed calculations and discussions of the viscous dissipation and the kinetic energy recovery are presented in Secs. IV and V, respectively.

II. NUMERICAL METHODOLOGY AND VALIDATIONS

A. Numerical method

The continuity and incompressible Navier-Stokes equations,

$$\nabla \cdot \boldsymbol{u} = 0, \tag{1}$$

$$\rho(\partial \boldsymbol{u}/\partial t + \boldsymbol{u} \cdot \nabla \boldsymbol{u}) = -\nabla p + \nabla \cdot (2\mu \boldsymbol{D}) + \sigma\kappa \boldsymbol{n}\delta_s, \tag{2}$$

are solved by using the classic fractional-step projection method, where $\boldsymbol{u}$ is the velocity vector, ρ is the density, p is the pressure, μ is the dynamic viscosity, and $\boldsymbol{D}$ is the deformation tensor defined as $D_{ij} = (\partial_j u_i + \partial_i u_j)/2$. In the surface tension term $\sigma\kappa\boldsymbol{n}\delta_s$, δ_s is a Dirac delta function, σ is the surface tension coefficient, κ is the local curvature, and the unit vector $\boldsymbol{n}$ is normal to the local interface.

As briefly discussed in the Introduction, the simulation of droplet collision by using the conventional VOF approach is strongly influenced by the mesh resolution near the interface. Specifically, a coarse mesh would induce "premature" coalescence of the droplets that are supposed to bounce off. Chen and Yang[39] developed a thickness-based adaptive mesh refinement method, and they could simulate droplet bouncing with a relatively smaller number of meshes because only the interface close to the interaction region was refined. However, the time step must be significantly decreased for numerical stability, thereby restricting the computational efficiency. Coyajee and Boersma[45] proposed a modified VOF approach which applies different marker functions to describe separate interfaces so as to avoid interface coalescence on a coarse mesh and has been validated for droplet bouncing on a liquid film[56] and binary droplet collision.[57] Kwakkel *et al.*[57] applied this approach to establish a droplet coalescence model by manually merging two interfaces at the experimentally verified gas film drainage time. The same idea of multiple marker functions was also implemented in Gerris by Hu *et al.*[40] to simulate binary droplet bouncing.

Following the approach of Coyajee and Boersma,[45] we use two volume fractions in the present simulation, namely, c_1 and c_2, to separately track the interface of each liquid droplet. To solve both the gas and liquid phases, the density and viscosity are constructed by the volume fraction as $\rho = (c_1 + c_2)\rho_l + (1 - c_1 - c_2)\rho_g$ and $\mu = (c_1 + c_2)\mu_l + (1 - c_1 - c_2)\mu_g$, in which the subscripts l and g denote the liquid and gas phases, respectively. The volume fraction $c_i (i = 1, 2)$ satisfies the advection equation

$$\partial c_i/\partial t + \nabla \cdot (c_i \boldsymbol{u}) = 0, \tag{3}$$

where $c_i = 1$ for the liquid phase, $c_i = 0$ for the gas phase, and $0 < c_i < 1$ for the gas-liquid interface. The present VOF method had been implemented in the open source code, Gerris,[43,44] featuring the 3D octree adaptive mesh refinement, the geometrical VOF interface reconstruction, and continuum surface force (CSF)

with height function curvature estimation. Gerris has been demonstrated to be competent for solving a wide range of multiphase problems.[23,26,27,39,54]

The two volume fractions independently describe the two droplets with no explicit conditions imposed for avoiding the overlap of interfaces. However, we found that, at least in the present simulations with the concerned controlling parameters leading to droplet bouncing, the interfaces belonging to the two droplets cannot contact and there is no overlap between the different VOF functions, which can be quantitatively verified by the measurement of the maximum excess of the combined volume fractions,[45] defined as $\max(c_1 + c_2 - 1)$. It is noted that this method would always enforce droplet bouncing for any droplet collision process and thus is applied in the present study for droplet bouncing cases that have been verified by experiments. More details about the comparison between the two marker functions method and the one marker function method are given in the Appendix.

B. Numerical specifications

The 3D computational domain and numerical specifications are illustrated in Fig. 1. The domain is $6D$ in length and $4D$ in both width and height, and all boundaries are specified with the free outflow boundary conditions. Two droplets of diameter D are specified to collide along the x-direction with a relative velocity, U, and zero velocities in the y- and z-directions. The x-velocity component for each droplet has the same magnitude of $U/2$ but opposite sign so that the linear momentum of the entire system remains zero. The x-z plane is established by the x-axis and the connection line denoted as OO', in which O and O' are the mass centers of the colliding droplets. The midpoint of OO' is located at the origin of the Cartesian coordinate system. It is noted that the x-z plane is always a plane of symmetry for the 3D colliding droplets. The deviation of the off-center collision from the head-on collision is qualified by χ, which is defined as the projection of OO' in the z-direction.

Choosing D, ρ_l, and σ as the basic units, we can nondimensionalize the eight relevant variables into five nondimensional parameters, such as We, Oh, B, ρ_g/ρ_l, and μ_g/μ_l, which are the Weber number, $We = \rho_l D U^2/\sigma$; the impact parameter, $B = \chi/D$; and the Ohnesorge number, $Oh = \mu_l/\sqrt{\rho_l \sigma D}$. In the present study concerning the collision between droplets in standard atmosphere environments, the gas-liquid density ratio and viscosity ratio (using tetradecane as an example) are $\rho_g/\rho_l = 1.61 \times 10^{-3}$ and $\mu_g/\mu_l = 7.94 \times 10^{-3}$, which has insignificant influence on droplet deformation and energy transfer according to previous studies.[26,27] Consequently, the present problem is completely controlled by the three parameters, We, Oh, and B for a fixed set of ρ_g/ρ_l and μ_g/μ_l. The nondimensional time is defined as $T = t/t_{osc}$, where t is the physical time and $t_{osc} = \sqrt{\rho_l D^3/\sigma}$ is proportional to the natural oscillation time of droplet.

In the present study, we used $6 \times 4 \times 4 = 96$ boxes with length L to constitute the entire computational domain, in which 6 boxes in the x-direction and 4 boxes in y- and z-directions, respectively. The droplet diameter is initialized as $D = L$. To improve computational efficiency, the computational domain is divided into three physical zones, namely, the gas, the droplet, and the interface, and each zone has its own mesh refinement level denoted by N, which corresponds to a minimum mesh size of $O(2^{-N})$. Accordingly, (N_g, N_d, N_i) is used to describe the refinement level in the three zones. A typical simulation run with the mesh refinement level (3, 5, 7) results in 514 204 grid points in the entire domain, which is equivalent to about 2.0×10^8 grid points if applying a uniform mesh with a size of $O(2^{-7})$. The interface zone is identified by the VOF function with $0 < c_1 + c_2 < 1$. Given the maximum mesh refinement level N_i, the minimum mesh size is $L/2^{N_i}$ in the interface zone. Then, the maximum numerical resolution[40] (MNR) of a droplet is defined as $\mathrm{MNR} = D/\left(L/\left(2^{N_i}+1\right)\right) = \left(2^{N_i}+1\right)D/L$. Thus, the maximum mesh refinement level $N = 7$ used in the present study corresponds to MNR = 129. It takes about 100 h of real time to run the simulation up to T = 2.0 on an Intel Xeon(R) E5-2630 processor with 16 cores.

C. Numerical validation and grid-dependence analysis

To validate the present numerical setup, the head-on droplet bouncing at two critical transition Weber numbers, corresponding to the so-called "soft" and "hard" collisions, and an off-center droplet bouncing are simulated and compared with the experimental results from Pan *et al.*[6] and Qian and Law,[7] respectively. Figure 2 shows the comparison between experimental images and simulation results. The presented simulation results are those having the most agreed droplet deformation with the experimental images, whereas the time discrepancies between them could serve as an indicator for the simulation performance.

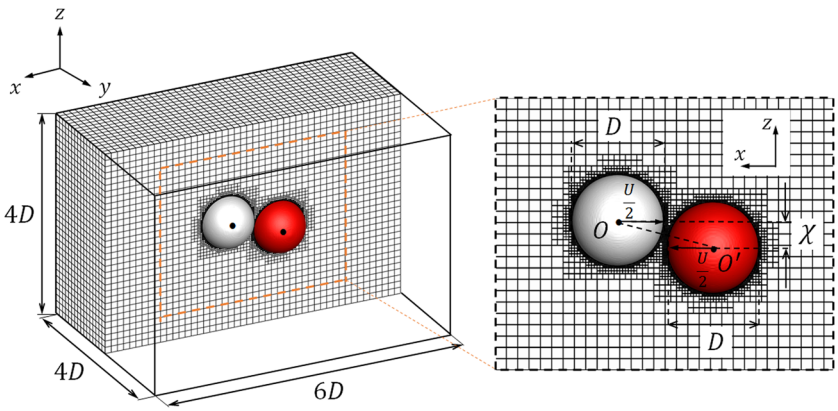

FIG. 1. Computational domain and setup for 3D simulation of off-center droplet collision.

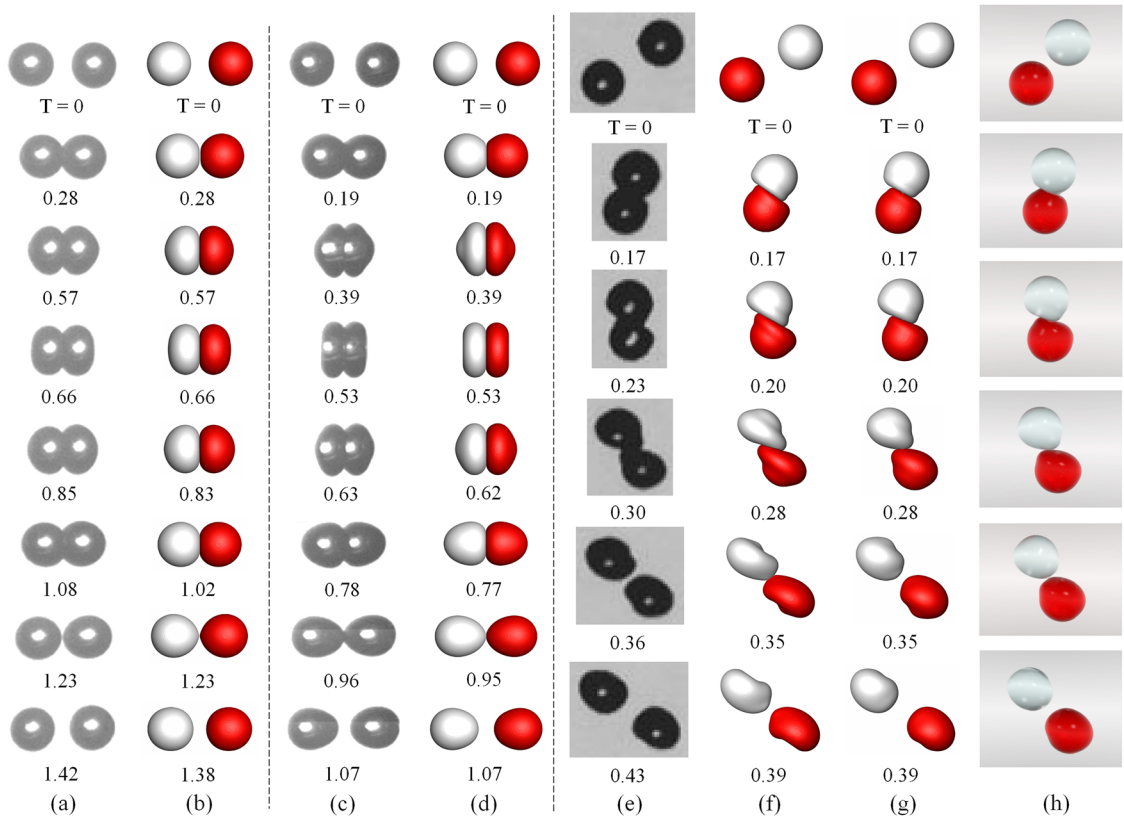

FIG. 2. Comparison between the experimental images and the simulation results for bouncing droplets of equal size. (a) The experiment images from Fig. 2 of Pan *et al.*[6] (head-on collision between tetradecane droplets in 1 atm air, R = 170.6 μm and V_0 = 0.243 m/s), (b) the simulation results at We = 2.3, Oh = 2.80 × 10^{-2}, and B = 0.0 (t_{osc} = 1.06 ms), (c) the experimental images from Fig. 3 of Pan *et al.*[6] (head-on collision between tetradecane droplets in 1 atm air, R = 167.6 μm and V_0 = 0.496 m/s), (d) the simulation results at We = 9.3, Oh = 2.78 × 10^{-2}, and B = 0.0 (t_{osc} = 1.03 ms), (e) the experiment images from Fig. 4(r) of Qian and Law[7] (off-center collision between tetradecane droplets in 1 atm air, We = 14.5, Re = 149.1, R = 180 μm, and B = 0.34), [(f)–(h)] the simulation results at We = 48.8 and Oh = 2.80 × 10^{-2} (t_{osc} = 1.06 ms) and (f) B = 0.72, (g) B = 0.82, and (h) B = 0.90 (adapted from Fig. 15 of Chen and Yang[39]). The physical time t is related to the computational time T by $T = t/t_{osc}$.

Figures 2(a) and 2(b) show the experimental images and the simulation results of the head-on (B = 0) droplet bouncing at We = 2.3 and Oh = 2.80 × 10^{-2} (t_{osc} = 1.06 ms),[6] respectively. The experimental and simulation times are nearly identical in early collision stages and begin to display slight discrepancies as time evolves in later stages. The time errors are generally less than 3% except it is about 5% at T = 1.08. Similarly, Figs. 2(c) and 2(d) show the experimental images and the simulation results of the head-on (B = 0) droplet bouncing at We = 9.3 and Oh = 2.78 × 10^{-2} (t_{osc} = 1.03 ms),[6] respectively. Again, the simulation agrees well the experiment and the time errors are less than 2%. The discrepancies between experiment and simulation may be attributed to the imperfect experimental conditions to be specified as follows. First, experimental images of droplet deformation show not perfectly symmetric with the small experimental error probably caused by the unavoidable disturbances of ambient gas flow to the droplets. Second, it might be caused by the experimental uncertainties in temporal resolution and the parameters measuring errors, for example, the droplets can be easily off-center in the direction perpendicular to the image plane. Furthermore, the above discussions about the imperfections of the experiments do not rule out the possible numerical errors.

Figure 2(e) shows the experimental images of off-center droplet bouncing adapted from Fig. 4(r) of Qian and Law,[7] who reported this case for We = 14.5, Oh = 2.80 × 10^{-2}, and B = 0.34. After a careful examination of their experimental images, we found that the droplets were very likely to undergo a nearly grazing collision with the impact parameter to be within 0.7–0.9. This may be caused by the possibly misplaced captions of Figs. 4(r) and 4(q) in their paper.[7] To further substantiate our claim, the simulation results by using We = 48.8, Oh = 2.80 × 10^{-2}, and B = 0.72 [used for Fig. 4(q) of Qian and Law[7]], B = 0.82, and B = 0.90 (used for Fig. 15 of Chen and Yang[39]) have been presented in Figs. 2(f)–2(h), respectively. These simulations can be considered as a sensitivity analysis of the impact parameter. It is seen that these simulations predict very similar droplet deformation to the experiment and that using B = 0.82 enables us to obtain quantitatively good agreement with the experiment. The time errors are about 10%, which is probably attributed to the experimental uncertainties in the measurement for time and collision parameters.[7]

Although a more detailed analysis on the experimental uncertainty of measured impact parameter is beyond the scope of the present study, a few remarks about this issue may be of use for future numerical studies that adopt those earlier experimental images for validation purpose. In Qian and Law,[7] the droplet sizes and velocity and thereby We and B were determined from the recorded images on a video recorder by using a strobelight synchronized with the droplet generator. The reported measurement errors of droplet size and impact parameter in Qian and Law[7] are about 10%. Gotaas *et al.*[58] have pointed out that such an experimental method in measuring impact parameter is generally not very accurate, and the measurement errors could be larger. Consequently, Gotaas *et al.*[58] proposed a more accurate and efficient aliasing method for continuous variation of impact parameter over its whole range from zero to unity.

The grid-independence analysis was performed for the validation case (a) of Fig. 2. The kinetic energy (KE) and surface energy (SE) of the liquid droplets are normalized by the initial total energy (TE) and compared for totally six different mesh refinement level sets (N_g, N_d, N_i), as shown in Fig. 3. The initial total energy is defined as $E_{k0} + \sigma S_0$, in which $E_{k0} = \pi We/24$ is the initial kinetic energy and $S_0 = 2\pi$ is the initial surface energy. By fixing the mesh refinement level of the gas and the droplet zones at $N_g = 2$ and $N_d = 4$, respectively, we can analyze the grid dependence of the interface zone, and the results show convergence up to T = 1.2 as increasing the mesh refinement level from $N_i = 7$ to $N_i = 8$. Similarly, the result comparison between (2, 4, 7) and (3, 5, 7) and further comparison between (2, 4, 8) and (4, 6, 8) also imply convergence of simulation with different mesh refinement levels of the gas and liquid zones. As a balance between computational cost and accuracy, the intermediate mesh refinement level of (3, 5, 7) has been used in the validation cases and all other simulations in Secs. III–V.

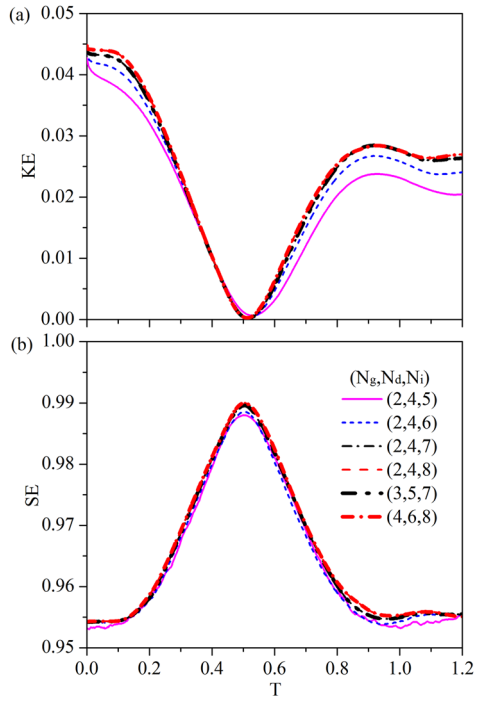

FIG. 3. Grid-independence analysis in terms of (a) the droplet kinetic energy (KE) and (b) the surface energy (SE) of the liquid droplets, which are normalized by the initial total energy ($E_{k0} + \sigma S_0$), for the validation case (a) shown in Fig. 2. (N_g, N_d, N_i) is used to describe the mesh refinement levels in each zone of the gas, the liquid, and the droplet interface.

III. PRELIMINARY ANALYSIS

A. Phenomenological description

The representative case of $We = 9.3$ and $Oh = 2.80 \times 10^{-2}$ at four different impact parameters, $B = 0.0$, 0.3, 0.6, and $B = 0.9$, has been used to phenomenologically describe the differences between the head-on and the off-center droplet bouncing, as shown in Fig. 4. The projection of droplet deformation on the symmetry (x-z) plane is shown in the first row of each case, in which the mass of the colliding droplet centers, O and O', is indicated by black solid points. To analyze the flow field within the droplets, the pressure contours and streamlines on the symmetry (x-z) plane and on the YOO' plane, where the y-axis and the line OO' lie, are shown in the second and third rows of each case in Fig. 4.

A prominent similarity between head-on and off-center collisions is the formation of a flat interaction region as the two droplets "squeeze" against each other. Although the dimension of this region and the duration of its existence both decrease notably with increasing the impact parameter, it always results in the locally enhanced capillary pressure around the rim of the interaction region where curvature is large. Once the inertia responsible for the "squeezing" is depleted, the deformed droplets are driven by the capillary pressure difference to bounce back, meanwhile, converting the surface energy back to the kinetic energy. Subsequently, the droplets experience several oscillation periods before completely recovering their original spherical shape, which happens at later times beyond those of Fig. 4. It is noted that the pressure distributions and streamlines on the YOO' plane for head-on and off-center collisions are qualitatively similar except the pressure amplitude for off-center collisions is smaller. The distinctive differences can be observed on the x-z plane for off-center collisions that the mass deviation in the z-direction results in the asymmetric pressure distribution for each droplet. In addition, the shear flow is clearly seen in the vicinity of the droplet interaction region only for off-center collisions on the symmetry (x-z) plane but not on the YOO' plane nor any plane of the head-on collision.

B. Energy budget

Based on the preliminary phenomenological observations, the entire collision process can be divided into three stages, namely, impacting, bouncing, and oscillating stages. The energy budget analysis is conducted based on liquid droplets,[4,6–8] as shown in Fig. 5, in which the time evolution of the kinetic energy (KE) and the surface energy (SE) of the liquid droplets are normalized by their initial total energy $E_{k0} + \sigma S_0$. T = 0.0 is defined as the time instant when $D_{OO'} = D$ for the first time as the two droplets approaching each other, where $D_{OO'}$ is the mass center distance shown in Fig. 5. It follows that the droplet impacting stage starts from T = 0.0 to the time instant with SE reaching its first maximum.

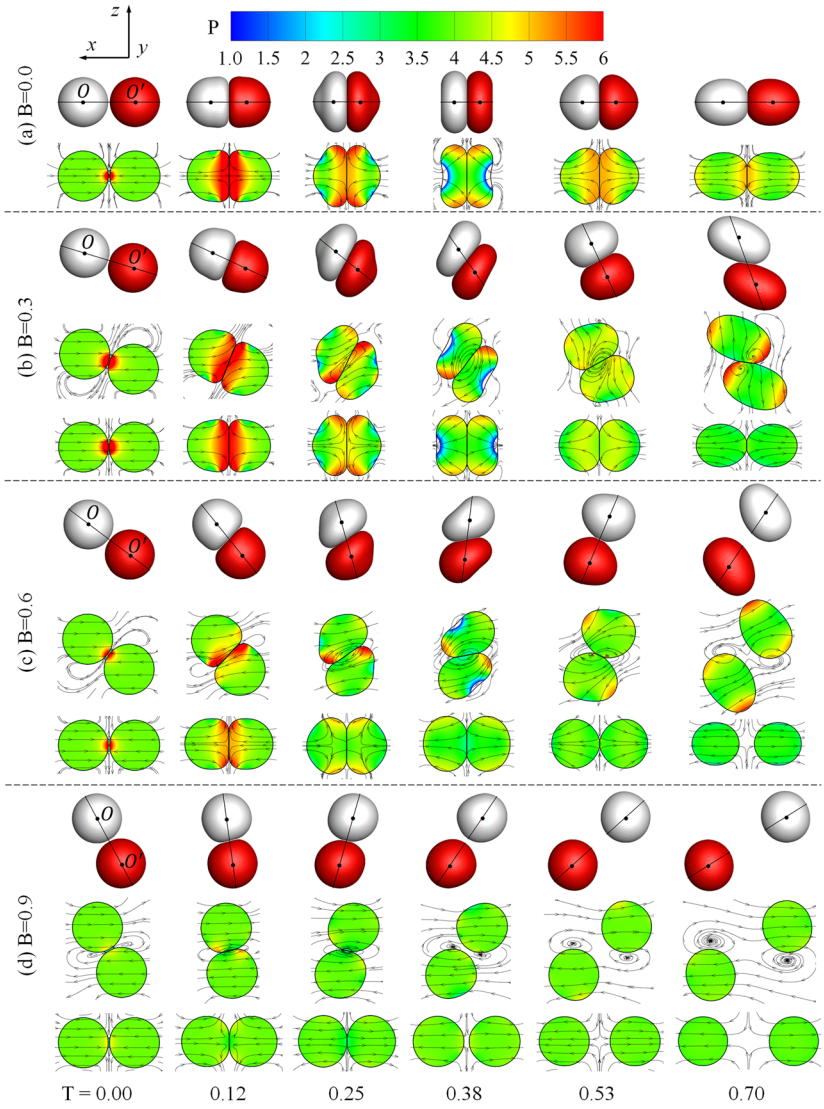

FIG. 4. Comparison of droplet deformation, pressure profiles, and streamlines between (a) head-on bounding (on the symmetry plane *x*-*z* only because it is axisymmetric) and [(b)–(d)] off-center bouncing (both on the symmetry plane *x*-*z* at first two rows and on the plane *YOO′* consisting of *y*-axis and mass center connection line *OO′* at the last row) for the representative case at $We = 9.3$ and $Oh = 2.78 \times 10^{-2}$.

The droplet bouncing stage then extends from the first local maximum to the first local minimum of SE, with the rest being the droplet oscillating stage. It is noted that the separation point (local maxima and minima of SE) and time duration for each stage are different between different impact parameters. The time evolution of $D_{OO'}$ shows that the increase in mass center distance for $B = 0.3$ is slowest with delayed droplet bouncing as the droplet entanglement time is prolonged for moderately off-center collisions, indicating a nonmonotonic variation with increasing B.

During the droplet impacting stage, both the total decrement of KE and the total increment of SE decrease monotonically with increasing B from 0.0 to 0.9. This is because increasing B tends to decrease the effective impact velocity ($U\sqrt{1-B^2}/2$) of colliding droplets along the mass center connection line and thereby results in a smaller droplet deformation with a smaller KE loss. During the droplet bouncing stage, the droplets start to bounce back with a decrease in SE and an increase in KE. Then, during the droplet oscillating stage, several apparent oscillations of SE and KE can be observed owing to the unbalanced capillary pressure shown in Fig. 4, particularly for the intermediate impact parameters at $B = 0.3$ and $B = 0.6$, and these oscillations are gradually attenuated by the viscous dissipation. An interesting observation throughout the entire droplet oscillating stage is that the KE for $B = 0.3$ is significantly lower than the other cases.

To further explain this observation, the total viscous dissipation energy (TVDE) of the liquid droplets normalized by the initial total energy is shown in Fig. 5. The TVDE is defined by

$$\mathrm{TVDE(T)} = \int_0^{\mathrm{T}} \left(\int_{V_l} \phi dV \right) d\mathrm{T}', \tag{4}$$

where V_l is the volume of liquid droplets and ϕ is the local viscous dissipation rate (VDR) given by[59]

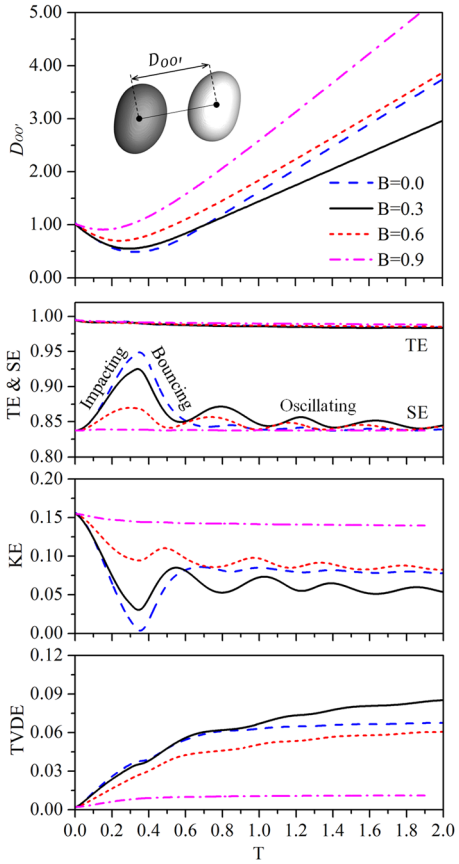

FIG. 5. Evolution of mass center distance $D_{OO'}$ and energy budget analysis of the off-center droplet bouncing for the representative case at *We* = 9.3 and *Oh* = 2.80 × 10^{-2}. The total energy (TE), the surface energy (SE), the kinetic energy (KE), and the total viscous dissipation energy (TVDE) of the liquid droplets are normalized by the initial total energy. The entire droplet collision process can be divided into three stages, namely, impacting, bouncing, and oscillating stages, based on the phenomenological observations.

$$\phi = \mu\left[2\left(\frac{\partial u}{\partial x}\right)^2 + 2\left(\frac{\partial v}{\partial y}\right)^2 + 2\left(\frac{\partial w}{\partial z}\right)^2 + \left(\frac{\partial u}{\partial y} + \frac{\partial v}{\partial x}\right)^2 + \left(\frac{\partial v}{\partial z} + \frac{\partial w}{\partial y}\right)^2 + \left(\frac{\partial w}{\partial x} + \frac{\partial u}{\partial z}\right)^2\right]. \quad (5)$$

As shown in Fig. 5, the TVDE of $B = 0.3$ during droplet bouncing and oscillating stages is the largest among all *B*s, indicating that the nonmonotonic kinetic energy recovery is caused by the nonmonotonic TVDE. To further understand the viscous dissipation of bouncing droplets in different stages, the temporal total viscous dissipation rate will be discussed in Sec. IV.

Furthermore, it is seen that the normalized total energy of droplets (TE = KE + SE + TVDE) is slightly lower than 1 and decreases with time, which can be explained as follows. First, the total energy (TE) is not exactly the total flow energy (TE′ = KE′ + SE + TVDE′ where the superscript prime denotes liquid and gas phases) because the contribution from the gas flow is neglected. Second, as

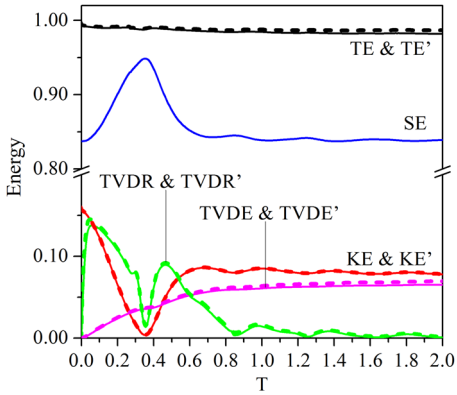

FIG. 6. Comparison of the evolution of the total energy (TE for the liquid droplets and TE′ for the total flow field), the surface energy (SE), the kinetic energy (KE and KE′), the total viscous dissipation rate (TVDR and TVDR′), and the total viscous dissipation energy (TVDE and TVDE′), respectively, by considering liquid phase only (solid lines) and both liquid and gas phases (dashed lines) for the representative case at *We* = 9.3, *Oh* = 2.78 × 10^{-2} and *B* = 0.0.

shown in Fig. 6, TE′ including the kinetic energy and viscous dissipation of both liquid and gas phases is slightly larger than that (TE) of the liquid phase only. This verifies that the energy budget of the gas flow is insignificant compared with that of the liquid droplets. Third, the normalized TE′ being still slightly lower than 1 might be due to the numerical dissipation. It is noted that the above is *a posteriori* examination of energy conservation because the energy conservation equation is not solved in the present simulation framework.

IV. VISCOUS DISSIPATION FOR OFF-CENTER COLLISIONS

A. Enhanced viscous dissipation for moderately off-center collisions

The total viscous dissipation rate (TVDR), defined as a volume integral $\int_{V_l} \phi dV$, and the contours of local VDR are illustrated in Figs. 7(a)–7(d) to explain the enhanced viscous dissipation at *B* = 0.3. It is seen that in all cases both the droplet impacting stage and the droplet bouncing stage contain a single peak of TVDR, whereas the droplet oscillating stage has several local maxima. The time instants corresponding to the first three local maxima of TVDR are denoted as T_1, T_2, and T_3.

A common feature during the droplet impacting stage is that it has the highest peak of TVDR and contributes to the majority of the overall viscous dissipation. As shown by the VDR contours at T_1 in Fig. 7(b), the local VDR is mainly distributed around the droplet interaction region where the liquid is both compressed along the OO' direction and expanded radially, displaying a boundary-layer-like internal flow that was also observed in previous theoretical analysis[46] and numerical simulations.[55] Furthermore, comparing the cases of different *B*s, it is seen that the TVDR decreases monotonically with increasing *B* during the droplet impacting stage. As the droplet deformation in this stage is inertia-dominant, this observation can be understood by an approximate estimation of the TVDE,

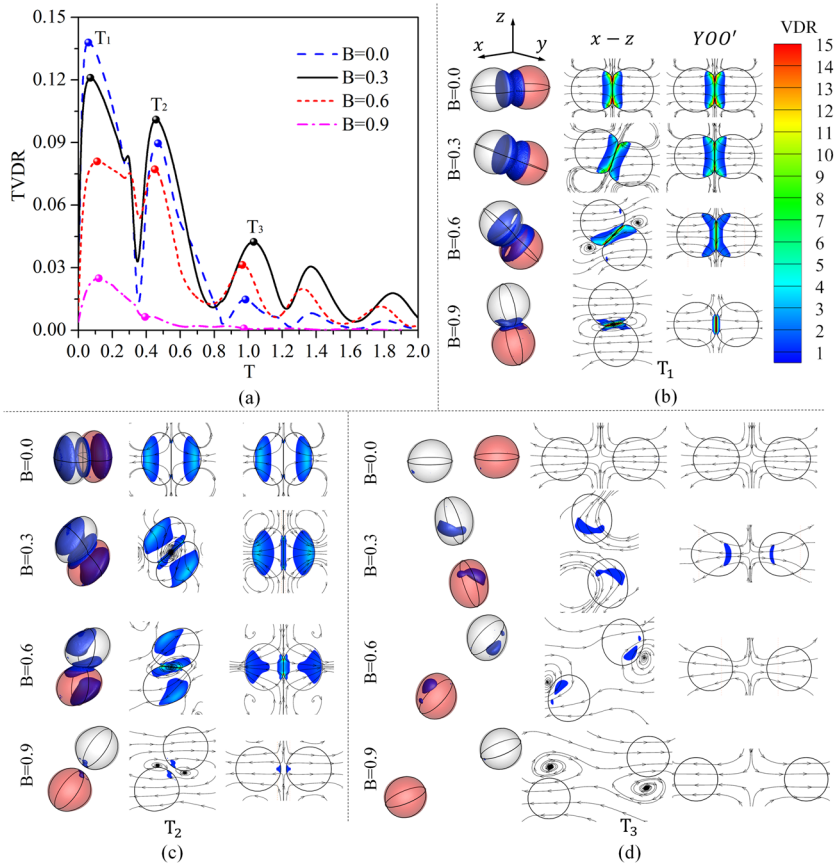

FIG. 7. Comparison of the (a) total viscous dissipation rate (TVDR) and [(b)–(d)] the contour of local viscous dissipation rate (VDR) at three chosen time instants, T_1, T_2, and T_3, for the representative case at *We* = 9.3 and *Oh* = 2.80 × 10^{-2}. The contours have been blanked with a low threshold value of 0.5 for clear comparison of the VDR concentration that shown both in three-dimensional and on the symmetry (*x*-*z*) and *YOO′* plane that defined in Fig. 4.

previously proposed by Jiang *et al.*[4] and Tang *et al.*,[8] as $\alpha E_k(B) = \alpha(1 - B^2)E_k(B = 0)$, where α is the viscous dissipation coefficient and $E_k(B)$ is the effective impact KE of the colliding droplets along the mass center connection line.

During the droplet bouncing stage, the droplets bounce back under the capillary pressure difference with the SE transferring into the KE. Figure 7(c) shows that at T_2 the VDR in the droplet interior being away from the interaction region decreases from maximum at $B = 0.0$ to nearly vanishing at $B = 0.9$. In this case, the TVDR can be estimated as $2\mu_l(\Delta SE)V_l/mD^2$, where ΔSE is the change of SE, the characteristic velocity is $u \sim \sqrt{2\Delta SE/m}$, and the characteristic length is D. Since ΔSE is closely related to the deformation of the droplets, the formula indicates that a larger droplet deformation in the droplet impacting stage would cause a larger TVDR in the droplet bouncing stage, which is consistent with the above observation. On the other hand, it is interesting to note that the local VDR emerges in the vicinity of the droplet interaction region only for off-center collisions but not for the head-on collision. This part of VDR is caused by the shear flow of off-center collisions as it becomes more prominent with increasing B. Apparently, the two parts of VDR, respectively, corresponding to the droplet deformation and the shear effect between the droplets, together form a competition mechanism which is responsible for the nonmonotonic variation of TVDR as a function of B.

As shown in Fig. 7(a), the fluctuations of TVDR during the droplet impacting stage emerge at small and intermediate impact parameters but not large impact parameters. Thereby, Fig. 8 shows the closeup of the fluctuation region and the corresponding

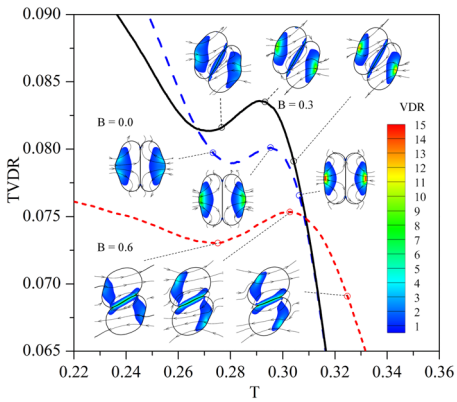

FIG. 8. The local fluctuations of total viscous dissipation rate (TVDR) and the contour of local viscous dissipation rate (VDR) (embedded subfigures) at three different time instants during the droplet impacting stage for the representative case at *We* = 9.3 and *Oh* = 2.80 × 10^{-2}.

contours of local viscous dissipation rate (VDR) for $B = 0.0$, 0.3, and 0.6. The locally enhanced TVDR is mainly located at the droplet interior being away from the interaction region with the convex interface tends to be flatten. That is consistent with the first peak of TVDR induced by the droplet impacting at initial stages, which can be understood as that the large viscous dissipation is generally accompanied by the intensive interface deformation with large curvature gradient change on the interface.

B. Quantitative explanation of the competition mechanism of VDRs

To further understand the competition mechanism between the VDR related to the droplet deformation and the VDR owing to the shear effects of off-center collisions, it is natural to separate the VDR terms in Eq. (5) into two parts, namely, the TVDR(N) related to the normal strains (the first three terms) and the TVDR(S) related to the shear strains (the last three terms). The shaded area in Figs. 9(a) and 9(b) shows the TVDR(N) and TVDR(S), respectively, in the droplet impacting and bouncing stages. The two representative time instants, T_n and T_s correspond to the local maximum of TVDR(N) in the impacting stage and the local maximum of TVDR(S) in the bouncing stage, respectively. As a reference, the TVDR(N) + TVDR(S) is plotted in the droplet oscillating stage. The case of $B = 0.9$ has been excluded from this discussion because it does not have a notable bouncing stage owing to the dominance of the shear effect, as indicated by Figs. 9(a) and 9(b).

It can be observed that for the small impact parameter at $B = 0.0$, the TVDR(N) is generally larger than the TVDR(S), whereas for the moderate impact parameters at $B = 0.3$ and 0.6, the TVDR(N) and TVDR(S) become equally significant to the TVDR. Specifically, during the droplet impacting stage and droplet bouncing stage, the TVDR(N) decreases monotonically with increasing B as shown in Fig. 9(a) and visualized by the local VDR contours at time T_n in Fig. 9(c), whereas the TVDR(S) increase monotonically from $B = 0.0$ to 0.6 as shown in Fig. 9(b) and the local VDR contours of Fig. 9(c) at time T_s. Therefore, we have demonstrated the competition mechanism through the different variation trends of TVDR(N) and TVDR(S) with increasing B, which accounts for the nonmonotonicity of TVDR being the largest around $B = 0.3$.

V. NONMONOTONIC KINETIC ENERGY DISSIPATION

A. The dependence of kinetic energy dissipation on *We* and *Oh*

In Lagrangian simulations of sprays[48–52] where the binary droplet collision is simplified as the collision between two mass points, the postcollision velocity of each droplet has to be determined from secondary models to serve as an input. Since the mass center trajectories always lie on the symmetry (x-z) plane, only four unknown velocities in the x- and z-directions are needed for a pair of colliding droplets. Given the conservations of the momentum in the x- and z-directions and the angular momentum in the x-z plane,

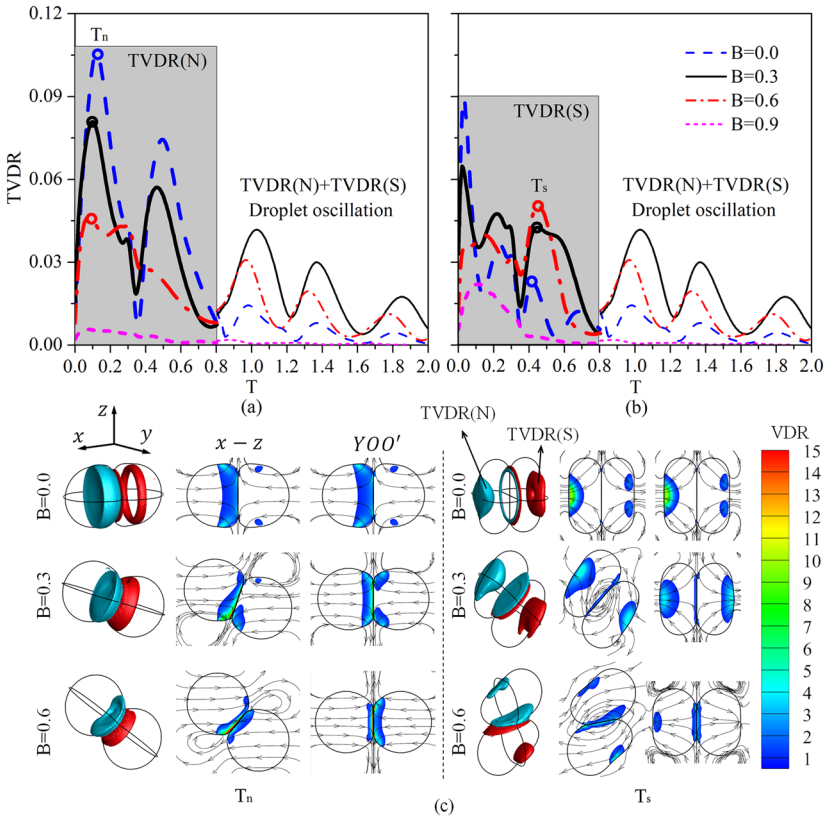

FIG. 9. Comparison of the total viscous dissipation rate (TVDR) induced by (a) the normal strains [TVDR (N)], (b) the shear strains [TVDR (S)], and (c) the contour of local VDR at time instants of T_n and T_s for the representative case at $We = 9.3$ and $Oh = 2.80 \times 10^{-2}$.

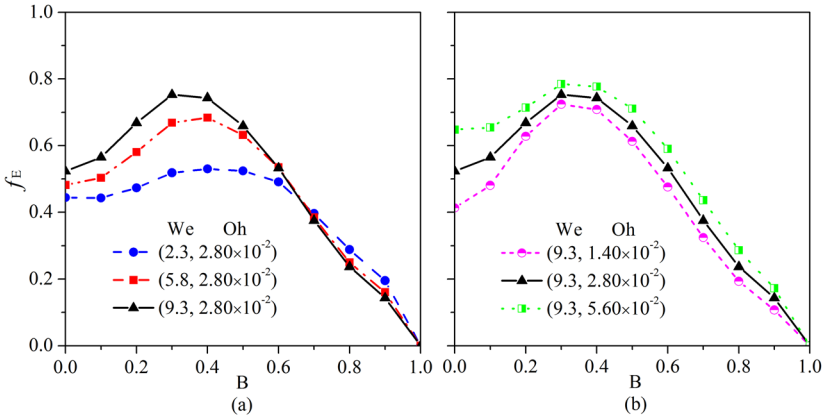

FIG. 10. Variation of the kinetic energy dissipation factor f_E with impact parameters B at different We and Oh.

one requires the kinetic energy dissipation factor f_E to close the equation system for the terminal velocity calculation. In the present study, we can compute f_E numerically with KE_b determined from the initial conditions and KE_a evaluated at the time instant when $D_{OO'} = 3D$, after which the KE_a is effectively unchanged for all cases. Accordingly, the kinetic energy recovery factor is calculated as $1 - f_E$.

Figure 10(a) shows f_E with varying B for different We. For small and intermediate B in the range of 0.0–0.7, f_E increases with We and the deviations of f_E among different We are enlarged at intermediate B. This is because the viscous dissipation induced by the droplet deformation is inertial-controlled and enhanced with increasing We. However, it is interesting to find that f_E is not sensitive with varying We for B in the range of 0.7–1.0. This indicates that We is a secondary factor to the viscous dissipation for near grazing collisions, which is likely the outcome of the shear effects dominating over the droplet deformation. Furthermore, the critical impact parameter B_{cr}, which is defined as the B corresponding to the local maximum of f_E (for fixed We and Oh), decreases slightly with increasing We. This is again attributed to the competition between the inertia and shear effects that increasing We causes greater relative importance of the droplet deformation on viscous dissipation so that the maximum f_E occurs at a smaller B_{cr}.

Figure 10(b) shows the variation of f_E as a function of B for different Oh. It is seen that f_E increases monotonically with Oh for all B, which is clearly attributed to the increased viscosity. However, the gaps among f_E of different Oh appear to be the largest at $B = 0.0$. The effect of Oh is further studied in Fig. 11, which shows that the increase in f_E is approximately linearly proportional to the increase in Oh/Oh_{ref} (or equivalently the ratio of the viscous coefficient μ_l), where Oh is normalized by a reference $Oh_{ref} = 1.4 \times 10^{-2}$. However, the slop for different impact parameters is not unity. This can be understood by the VDR estimation in Eq. (5) that the viscous dissipation is a synergistic effect that is influenced not only by the viscous coefficient but also by the velocity gradients related to the internal flow and the integral droplet interaction time. Furthermore, the slops for different impact parameters seem to be consistent except the cases of $B = 0.0$. This is likely to reflect the additional dissipation effect associated with the distinct droplet deformation, which occurs as a byproduct of changing viscosity when the impact inertia is large at small B.

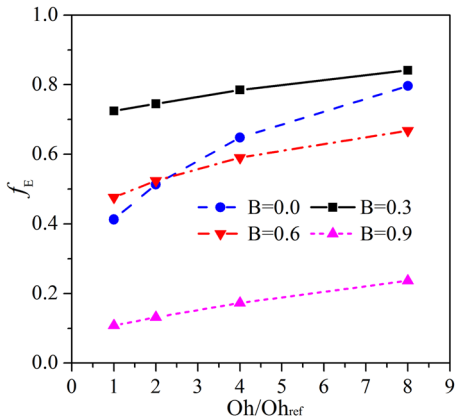

FIG. 11. Variation of the kinetic energy dissipation factor f_E with Oh for the representative We = 9.3.

B. An approximate fitting formula

The above results have demonstrated an overall general trend of the nonmonotonic kinetic energy recovery and viscous dissipation for different We and Oh. Here, we propose an approximate fitting formula of f_E/f_{E0} to serve for Lagrangian simulations of spray based on the following considerations. First, this formula reflects the most important finding of the present study that the kinetic energy dissipation factor varies nonmonotonically with the impact parameter. Second, the functional dependence of the factor on We and Oh for head-on collisions, namely, $f_{E0}(We, Oh) = f_E(We, Oh, B = 0)$, has been comprehensively studied by Zhang and Zhang.[55] The normalized f_E by f_{E0} for different We and Oh is shown in Fig. 12(a) with scattering points. Thus, following their conclusions, we incorporate the additional impact parameter effect to attain a simple fitting formula

$$f_E/f_{E0} = a(B - B_{cr})^2 + b \tag{6}$$

to describe the nonmonotonic variation of f_E/f_{E0} with increasing B. The parabola on the $f_E/f_{E0} - B$ plane must cross the point of (0, 1) by

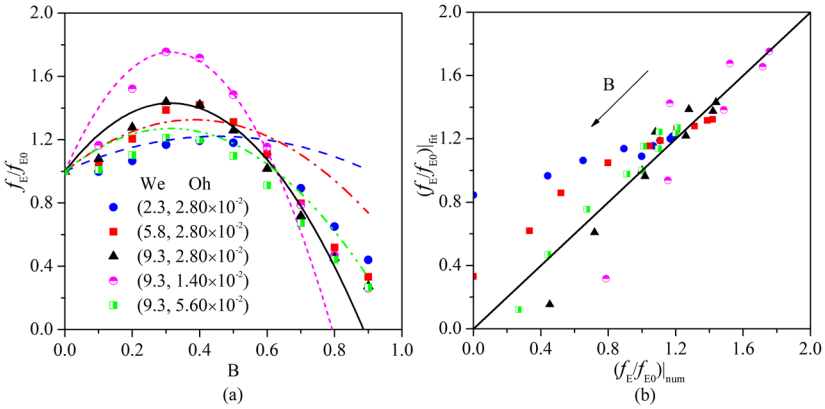

FIG. 12. Comparison of (a) the kinetic energy dissipation factor f_E normalized by f_{E0} that obtained from the previous study[55] (scattering points of numerical results and lines of fitting formula) and (b) deviation of f_E/f_{E0} between numerical (horizontal) and fitting (vertical) results.

definition, yielding $a = (1 - b)/B_{cr}{}^2 < 0$, and the point of (B_{cr}, b) to reflect the existence of a maximum value on the parabola. We found that the proposed approximate formula with $B_{cr} = 0.5–0.2(We/10)$ and $b = 0.83 + 0.3(We/10) + 0.9(Oh/10^{-2})^{-1}$ can satisfactorily fit our numerical data for the concerned parameter space of $We = 2.3–9.3$ and $Oh = 1.4 \times 10^{-2}$ to 5.6×10^{-2}, as the lines shown in Fig. 12(a).

Figure 12(b) shows the comparison between numerical and fitting results, indicating that they are in good agreement at small and intermediate B in the range of 0.0–0.6 although they deviate at large B where the small f_E/f_{E0} is insignificant to the practical purpose. The more accurate high-order fitting formula merits future investigations, given more numerical or experimental data, but is beyond the scope of the present study.

VI. CONCLUSIONS

Two droplets bouncing undergoing off-center collisions were simulated in the present study by using a modified VOF approach with two marker functions and validated against experiments of both head-on and off-center collisions. The implementation of multiple marker functions helped to avoid the unphysical numerical coalescence under relatively coarse mesh so that it allows us to study the 3D off-center droplet bouncing with substantially increased computational efficiency.

The analysis of mass center trajectory demonstrates that the droplet entanglement time is prolonged for moderately off-center collisions. A nonmonotonic kinetic energy recovery with varying impact parameters was observed, which is attributed to the enhanced viscous dissipation of moderately off-center collisions.

The present study has strived to unveil and interpret the nonmonotonicity. Specifically, as increasing B from 0 to 1, the VDR in the droplet interior being away from the interaction region decreases because of the reduced droplet deformation, whereas the VDR in the vicinity of the droplet interaction region increases owing to the enhanced droplet shear flow. The competition mechanism between these two parts of VDR accounts for the enhanced viscous dissipation at intermediate B in the early stages of droplet collision, while the enhanced droplet oscillation owing to the unbalanced capillary pressure distributions results in the further increase of viscous dissipation at intermediate B in the late periods of droplet oscillation. This mechanism can also be understood as the competition between VDR induced by normal strains and shear strains, which quantitatively verifies our discussions and helps us understand the viscous dissipation for off-center droplet collisions.

The nonmonotonic kinetic energy recovery has been quantitatively verified to be a general phenomenon for various We and Oh. The total viscous dissipation is understood as a concerted work by the liquid viscosity, internal-flow-induced droplet deformation, and droplet interaction time. A correlation formula, $f_E/f_{E0} = a(B - B_{cr})^2 + b$, has been proposed for $We = 2.3–9.3$ and $Oh = 1.4 \times 10^{-2}$ to 5.6×10^{-2}. This formula could be useful for the droplet collision modeling in the Lagrangian simulation of sprays, particularly under the elevated gas pressure in the real combustion engines.

ACKNOWLEDGMENTS

The work was supported partly by the Hong Kong RGC/GRF (Grant Nos. PolyU 152217/14E and PolyU 152651/16E) and partly by the Hong Kong Polytechnic University (Grant No. G-YBXN). We are grateful to the State Key Laboratory of Engines of Tianjin University for an "Open Fund" (Grant No. K2018-12) and to Dr. Zhenyu Zhang for his insightful advices for result discussion.

APPENDIX: COMPARISON OF VOF METHODS

As discussed in Sec. II, for the conventional volume-of-fluid (VOF) method with one marker function, the mesh size resolving the interfaces between two colliding droplets must be sufficiently small in order to capture the outcome of bouncing; otherwise, the unphysical interface coalescence would occur numerically. However for the modified VOF method with two marker functions, the unphysical interface coalescence can be avoided even with the coarse mesh.

To compare the differences between these two VOF methods, the time evolution of the droplet deformation for $We = 2.3$, $Oh = 2.80 \times 10^{-2}$, and $B = 0.0$ is shown in Fig. 13(a), which involves three different cases: one marker function with fine mesh, two marker functions with fine mesh, and two marker functions with coarse mesh. The results show that the droplet deformations collapse with each other for different interface mesh resolution and marker functions. Figure 13(b) further shows the evolution of the central interface distance h_c for the above three cases, where h_c

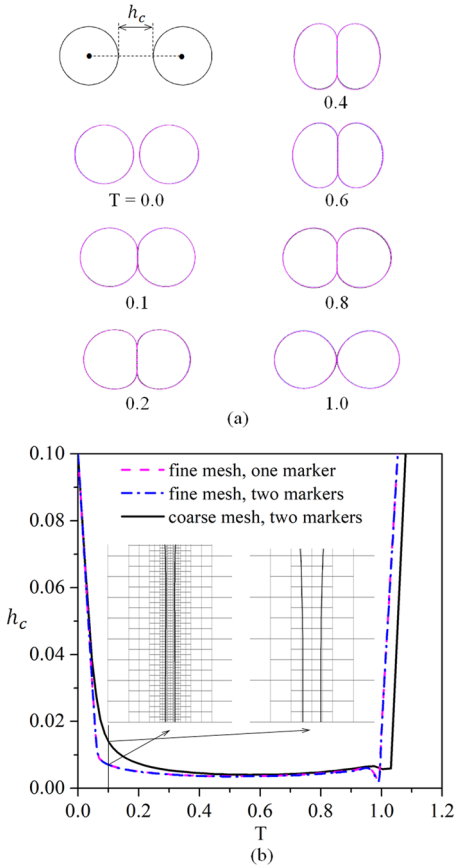

FIG. 13. Comparison of (a) the droplet deformation and (b) the central interface distance, h_c, of colliding droplets by using different interface mesh resolution and marker functions for the case at We = 2.3, Oh = 2.80 × 10^{-2}, and B = 0.0.

is defined as the minimum distance between two colliding interfaces along the mass center connection line, as illustrated in the first image of Fig. 13(a). The evolutions of h_c for the one marker function and the two marker functions, both with fine mesh, are identical, while there show some deviations from the two marker functions with coarse mesh. We argue that the VOF method by applying two marker functions with coarse mesh is sufficiently accurate to simulate droplet bouncing in the present study for the following reasons. One is that the minimum h_c at about T = 0.6 is still preserved. Moreover, the deviations of h_c are in the order of $O(10^{-2})$ compared with the droplet diameter D and effectively only cause a more time offset which does not affect the droplet deformation or other physics during the process.

Figure 14 shows the evolution of droplet interface positions and central interface distance h_c on the symmetry plane (x-z) at four chosen time instants, T_1, T_2, T_3, and T_4 for the case shown in Fig. 13. It indicates that the droplet interfaces could be advected in the two immediately neighboring interface cells. The minimum central interface distance h_c = 0.004 occurs at about T_4 = 0.6, which is nearly half of the minimum mesh size of $1/2^7 \approx 0.008$. It indicates that the minimum central interface distance h_c can be smaller than the minimum mesh size in the present simulation.

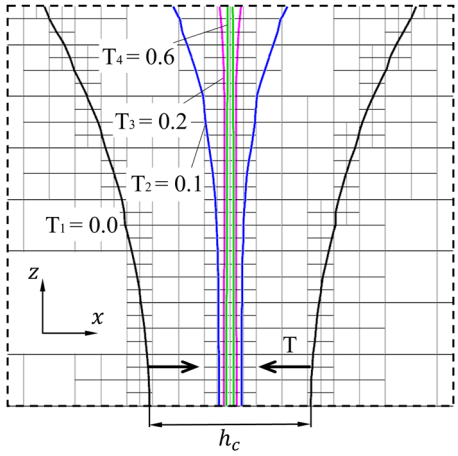

FIG. 14. Evolution of interface positions and central interface distance h_c on the symmetry plane (x-z) at We = 2.3, Oh = 2.80 × 10^{-2}, and B = 0.0.

REFERENCES

[1] N. Ashgriz and J. Poo, "Coalescence and separation in binary collisions of liquid drops," J. Fluid Mech. **221**, 183 (1990).
[2] G. Brenn, "Droplet collision," in *Handbook of Atomization and Sprays* (Springer, Berlin, 2011).
[3] O. Jayaratne and B. J. Mason, "The coalescence and bouncing of water drops at an air/water interface," Proc. R. Soc. London, Ser. A **280**, 545 (1964).
[4] Y. Jiang, A. Umemura, and C. Law, "An experimental investigation on the collision behaviour of hydrocarbon droplets," J. Fluid Mech. **234**, 171 (1992).
[5] M. Orme, "Experiments on droplet collisions, bounce, coalescence and disruption," Prog. Energy Combust. Sci. **23**, 65 (1997).
[6] K.-L. Pan, C. K. Law, and B. Zhou, "Experimental and mechanistic description of merging and bouncing in head-on binary droplet collision," J. Appl. Phys. **103**, 064901 (2008).
[7] J. Qian and C. K. Law, "Regimes of coalescence and separation in droplet collision," J. Fluid Mech. **331**, 59 (1997).
[8] C. Tang, P. Zhang, and C. K. Law, "Bouncing, coalescence, and separation in head-on collision of unequal-size droplets," Phys. Fluids **24**, 022101 (2012).
[9] E. Villermaux and B. Bossa, "Single-drop fragmentation determines size distribution of raindrops," Nat. Phys. **5**, 697 (2009).
[10] E. Villermaux and B. Bossa, "Size distribution of raindrops," Nat. Phys. **6**, 232 (2010).
[11] J. B. Heywood, *Internal Combustion Engine Fundamentals* (McGraw-Hill, New York, 1988).
[12] W. A. Sirignano, *Fluid Dynamics and Transport of Droplets and Sprays* (Cambridge University Press, 1999).
[13] S. L. Anna, "Droplets and bubbles in microfluidic devices," Annu. Rev. Fluid Mech. **48**, 285 (2016).
[14] S.-Y. Teh, R. Lin, L.-H. Hung, and A. P. Lee, "Droplet microfluidics," Lab Chip **8**, 198 (2008).
[15] J. C. Bird, R. Dhiman, H.-M. Kwon, and K. K. Varanasi, "Reducing the contact time of a bouncing drop," Nature **503**, 385 (2013).
[16] T. Liu and C.-J. Kim, "Turning a surface superrepellent even to completely wetting liquids," Science **346**, 1096 (2014).
[17] Y. Liu, M. Andrew, J. Li, J. M. Yeomans, and Z. Wang, "Symmetry breaking in drop bouncing on curved surfaces," Nat. Commun. **6**, 10034 (2015).
[18] Y. Liu, L. Moevius, X. Xu, T. Qian, J. M. Yeomans, and Z. Wang, "Pancake bouncing on superhydrophobic surfaces," Nat. Phys. **10**, 515 (2014).
[19] Y. Lu, S. Sathasivam, J. Song, C. R. Crick, C. J. Carmalt, and I. P. Parkin, "Robust self-cleaning surfaces that function when exposed to either air or oil," Science **347**, 1132 (2015).

[20]D. Richard, C. Clanet, and D. Quéré, "Surface phenomena: Contact time of a bouncing drop," Nature **417**, 811 (2002).
[21]W. Ristenpart, J. Bird, A. Belmonte, F. Dollar, and H. Stone, "Non-coalescence of oppositely charged drops," Nature **461**, 377 (2009).
[22]H. P. Kavehpour, "Coalescence of drops," Annu. Rev. Fluid Mech. **47**, 245 (2015).
[23]X. Chen, D. Ma, and V. Yang, "Collision outcome and mass transfer of unequal-sized droplet collision," in *50th AIAA Aerospace Sciences Meeting* (AIAA, 2012).
[24]D. Liu, P. Zhang, C. K. Law, and Y. Guo, "Collision dynamics and mixing of unequal-size droplets," Int. J. Heat Mass Transfer **57**, 421 (2013).
[25]K. Sun, P. Zhang, M. Jia, and T. Wang, "Collision-induced jet-like mixing for droplets of unequal-sizes," Int. J. Heat Mass Transfer **120**, 218 (2018).
[26]C. Tang, J. Zhao, P. Zhang, C. K. Law, and Z. Huang, "Dynamics of internal jets in the merging of two droplets of unequal sizes," J. Fluid Mech. **795**, 671 (2016).
[27]X. Xia, C. He, D. Yu, J. Zhao, and P. Zhang, "Vortex-ring-induced internal mixing upon the coalescence of initially stationary droplets," Phys. Rev. Fluids **2**, 113607 (2017).
[28]K. Krishnan and E. Loth, "Effects of gas and droplet characteristics on drop-drop collision outcome regimes," Int. J. Multiphase Flow **77**, 171 (2015).
[29]L. Reitter, M. Liu, J. Breitenbach, K.-L. Huang, D. Bothe, G. Brenn, K.-L. Pan, I. Roisman, and C. Tropea, "Experimental and computational investigation of binary drop collisions under elevated pressure," in 28th European Conference on Liquid Atomization and Spray System, 2017.
[30]Z. Zhang, Y. Chi, L. Shang, P. Zhang, and Z. Zhao, "On the role of droplet bouncing in modeling impinging sprays under elevated pressures," Int. J. Heat Mass Transfer **102**, 657 (2016).
[31]Z. Zhang and P. Zhang, "Cross-impingement and combustion of sprays in high-pressure chamber and opposed-piston compression ignition engine," Appl. Therm. Eng. **144**, 137 (2018).
[32]Z. Zhang and P. Zhang, "Modeling kinetic energy dissipation of bouncing droplets for Lagrangian simulation of impinging sprays under high ambient pressure," Atomization Sprays **28**, 673 (2018).
[33]K. H. Al-Dirawi and A. E. Bayly, "A new model for the bouncing regime boundary in binary droplet collisions," Phys. Fluids **31**, 027105 (2019).
[34]S. Farokhirad, J. F. Morris, and T. Lee, "Coalescence-induced jumping of droplet: Inertia and viscosity effects," Phys. Fluids **27**, 102102 (2015).
[35]R. Attarzadeh and A. Dolatabadi, "Coalescence-induced jumping of micro-droplets on heterogeneous superhydrophobic surfaces," Phys. Fluids **29**, 012104 (2017).
[36]X. Tang, A. Saha, C. K. Law, and C. Sun, "Bouncing drop on liquid film: Dynamics of interfacial gas layer," Phys. Fluids **31**, 013304 (2019).
[37]X. Tang, A. Saha, C. K. Law, and C. Sun, "Bouncing-to-merging transition in drop impact on liquid film: Role of liquid viscosity," Langmuir **34**, 2654 (2018).
[38]F. Blanchette, "Modeling the vertical motion of drops bouncing on a bounded fluid reservoir," Phys. Fluids **28**, 032104 (2016).
[39]X. Chen and V. Yang, "Thickness-based adaptive mesh refinement methods for multi-phase flow simulations with thin regions," J. Comput. Phys. **269**, 22 (2014).
[40]C. Hu, S. Xia, C. Li, and G. Wu, "Three-dimensional numerical investigation and modeling of binary alumina droplet collisions," Int. J. Heat Mass Transfer **113**, 569 (2017).
[41]B. Sakakibara and T. Inamuro, "Lattice Boltzmann simulation of collision dynamics of two unequal-size droplets," Int. J. Heat Mass Transfer **51**, 3207 (2008).
[42]F. H. Zhang, E. Q. Li, and S. T. Thoroddsen, "Satellite formation during coalescence of unequal size drops," Phys. Rev. Lett. **102**, 104502 (2009).
[43]S. Popinet, "Gerris: A tree-based adaptive solver for the incompressible Euler equations in complex geometries," J. Comput. Phys. **190**, 572 (2003).
[44]S. Popinet, "An accurate adaptive solver for surface-tension-driven interfacial flows," J. Comput. Phys. **228**, 5838 (2009).
[45]E. Coyajee and B. J. Boersma, "Numerical simulation of drop impact on a liquid–liquid interface with a multiple marker front-capturing method," J. Comput. Phys. **228**, 4444 (2009).
[46]P. Zhang and C. K. Law, "An analysis of head-on droplet collision with large deformation in gaseous medium," Phys. Fluids **23**, 042102 (2011).
[47]J. Li, "Macroscopic model for head-on binary droplet collisions in a gaseous medium," Phys. Rev. Lett. **117**, 214502 (2016).
[48]R. Aumann, M. McCracken, and J. Abraham, "An evaluation of a composite model for predicting drop-drop collision outcomes in multidimensional spray computations," in *SAE Transactions* (SAE International, 2002).
[49]P. Brazier-Smith, S. Jennings, and J. Latham, "The interaction of falling water drops: Coalescence," Proc. R. Soc. London, Ser. A **326**, 393 (1972).
[50]J.-P. Estrade, H. Carentz, G. Lavergne, and Y. Biscos, "Experimental investigation of dynamic binary collision of ethanol droplets—A model for droplet coalescence and bouncing," Int. J. Heat Fluid Flow **20**, 486 (1999).
[51]P. J. O'Rourke, "Collective drop effects on vaporizing liquid sprays," Ph.D. thesis, Princeton University, 1981.
[52]S. L. Post and J. Abraham, "Modeling the outcome of drop–drop collisions in Diesel sprays," Int. J. Multiphase Flow **28**, 997 (2002).
[53]A. Munnannur and R. D. Reitz, "Comprehensive collision model for multidimensional engine spray computations," Atomization Sprays **19**, 597 (2009).
[54]X. Chen, D. Ma, P. Khare, and V. Yang, "Energy and mass transfer during binary droplet collision," in *49th AIAA Aerospace Sciences Meeting* (AIAA, 2011).
[55]Z. Zhang and P. Zhang, "Kinetic energy recovery and interface hysteresis of bouncing droplets after inelastic head-on collision," Phys. Fluids **29**, 103306 (2017).
[56]Z. Mohamed-Kassim and E. K. Longmire, "Drop impact on a liquid–liquid interface," Phys. Fluids **15**, 3263 (2003).
[57]M. Kwakkel, W.-P. Breugem, and B. J. Boersma, "Extension of a CLSVOF method for droplet-laden flows with a coalescence/breakup model," J. Comput. Phys. **253**, 166 (2013).
[58]C. Gotaas, P. Havelka, H. A. Jakobsen, and H. F. Svendsen, "Evaluation of the impact parameter in droplet-droplet collision experiments by the aliasing method," Phys. Fluids **19**, 102105 (2007).
[59]F. M. White and I. Corfield, *Viscous Fluid Flow* (McGraw-Hill, New York, 2006).